



Modeling of three-way catalytic converter performance with exhaust mixture from natural gas-fueled engines



Fan Zeng, Keith L. Hohn*

Department of Chemical Engineering, Kansas State University, Durland Hall, Manhattan, KS 66506, USA

ARTICLE INFO

Article history:

Received 4 August 2015

Received in revised form

30 September 2015

Accepted 2 October 2015

Keywords:

Natural gas engine

Three-way catalytic converter modeling

Air to fuel ratio

NO reduction

Methane oxidation

Sensitivity analysis

ABSTRACT

The ability of a three-way catalytic converter (TWC) to treat the exhaust from a natural-gas fueled engine was evaluated by numerical simulation. A comprehensive and thermodynamically consistent surface reaction mechanism describing the surface reactions in the TWC was built by compiling elementary-step reaction kinetics involving CH_4 , CO , formaldehyde, NO , NH_3 and N_2O from literature sources. The reaction parameters are taken from literatures and fitting calculations. The mechanism was implemented in a one-dimensional PFR model describing a single channel of the catalyst. The simulation results were evaluated by comparison with field data collected from a TWC operated isothermally at steady-state. The model predicted the major trends in conversion/formation of all species in the TWC over a wide range of air to fuel ratios. Sensitivity analysis was utilized to study the key reaction steps that impact the exhaust emission mole fraction. It was found that methane, NO , CO and formaldehyde are most sensitive to the corresponding adsorption steps, while NH_3 and N_2O are sensitive to the reactions that relate to their formations, such as reactions involving surface hydrogen atoms for NH_3 and NO for N_2O .

© 2015 Elsevier B.V. All rights reserved.

1. Introduction

In response to stringent environmental regulations, the automotive industry has conducted a substantial amount of research into three-way catalytic converter (TWC) systems to simultaneously remove unburned hydrocarbon (HC), NO_x and CO from the exhaust from gasoline-fueled engines [1]. This includes the development of TWC converter microkinetic models that comprehensively describe the catalytic chemistry on a molecular level [2,3]. Recently, there is an interest in using TWC for treating the exhaust from natural gas engines due to the New Source Performance Standards promulgated by EPA in January, 2008. In addition, natural gas is the world's fastest growing major energy source and is projected to rise into second place among energy sources by 2040 [4]. For this reason it will be increasingly important to explore catalytic processes to reduce emissions from natural gas-powered engines. The models developed for gasoline engines are insufficient for modeling a TWC for treating emissions from natural gas engines, since they lack detailed chemistry for methane.

The core of the TWC is a multi-channeled ceramic or metallic monolith. A washcoat (catalyst carrier) containing finely dispersed

noble metals (Pt, Pd, Rh) and ceria is coated on the wall of the channel, through which exhaust gases flows. The noble metals are the active sites, catalyzing both oxidation and reduction [5]. Ceria is added because of its structural properties, its reversibility of sulfur poisoning and its rapid kinetics of oxygen storage and release [6], however this effect is not considered in the current steady state model. The exhaust emission condition is quantized using the normalized air to fuel ratio as

$$\lambda = \frac{\text{AF}_{\text{realistic}}}{\text{AF}_{\text{stoichiometric}}}$$

Therefore, $\lambda > 1$ corresponds to fuel lean conditions while $\lambda < 1$ corresponds to fuel rich conditions. It is widely accepted that the air to fuel ratio has a great impact on the TWC ability to efficiently remove CO and NO_x from the exhaust. The efficiency reaches a maximum around the stoichiometric condition ($\lambda = 1$) [7]. Research on gasoline [8] and natural gas engines [9] both indicate that there is a trade-off between NO and CO conversion. Fuel-rich conditions produce high NO conversion but low CO conversion, while the opposite trend is noted at fuel-lean condition. Only at air to fuel ratios very close to the stoichiometric point can both components be reduced significantly.

Methane oxidation chemistry over noble metals, particularly platinum and palladium, has been extensively studied. Activation of the C–H bond is generally considered as the rate limiting step for methane combustion and two activation mechanism were pro-

* Corresponding author.

E-mail address: hohn@ksu.edu (K.L. Hohn).

posed on these two metals. Burch and coworker [10] proposed that Pt activates the C–H bond of methane by dissociative adsorption of methane at vacant metal sites, fully covered with oxygen species cannot activate C–H bond. By contrast, Pd is much more effective than Pt at lean conditions, $\text{Pd}^{2+}\text{O}^{2-}$ ions on PdO surface can more easily activate the C–H bond and PdO is considered as the active phase [11]. The reversible transformation between PdO and metallic Pd is well observed and a correlation has been found between this transformation and methane oxidation activity [12]. Miller and Malatpure [13] indicated that methane total oxidation is correlated to the density of $\text{PdO-Pd}(\cdot)$ (\cdot is an O-vacancy) site pairs: if the PdO is overstabilized by the support (CeO_2), then it cannot be partially reduced to $\text{Pd}(\cdot)$ to form the site pairs required by the reaction, and activity is decreased. Even though Pd exhibited better methane oxidation performance at lean condition, the complex transformation between metallic palladium and the metal oxide complicates the kinetic modeling of methane oxidation which should include the PdO formation [14].

Methane chemistry over platinum has been investigated for autothermal reforming [15], catalytic partial oxidation [16] and complete oxidation [17]. Burch and Loader compared the methane combustion over $\text{Pt/Al}_2\text{O}_3$ and $\text{Pd/Al}_2\text{O}_3$, and showed that at higher methane conversions with stoichiometric or rich mixtures $\text{Pt/Al}_2\text{O}_3$ is a more active catalyst. They also concluded that platinum can be a more effective catalyst than palladium for methane combustion under real conditions [18].

Lyubovsky et al. studied the methane catalytic combustion over Pt-group catalyst both in fuel lean and fuel rich conditions [19]. They showed that the surface is covered with oxygen when reacting with a fuel-lean mixture, while it is covered with CO and H when reacting with a fuel-rich mixture. They suggested that the catalyst had a different state under fuel lean and fuel rich conditions, which resulted in different mechanisms for the interaction of methane with the catalyst. Buyevskaya [20] investigated the role of surface coverage on methane partial oxidation by flowing CH_4 over an initial O_2 -treated catalyst. The initial CO_2 selectivity was 100% but the major product produced shifted from CO_2 to CO as the surface oxygen was consumed, indicating that an oxygen-rich catalyst surface promoted the CO_2 formation, while an oxygen-lean surface leads to CO formation.

Due to platinum's high activity for methane oxidation and NOx reduction, detailed elementary-step mechanisms for methane catalytic partial oxidation and NO reduction have been reported on platinum. Hickman and Schmidt [21] proposed a 19-elementary-step model for methane oxidation under methane-rich conditions on Pt and Rh surfaces. The dissociative adsorption of methane was grouped into a single step and was not reversible. The mechanism indicated that the H_2 and CO are primary products. Deutschmann et al. have developed microkinetic models for methane oxidation on rhodium that can be used to simulate steady-state partial oxidation [22] and transient behavior of catalytic monoliths [23]. Vlachos [24] used a hybrid parameter estimation methodology, based on experimental data, semi-empirical methods and first principle density function theory to estimate reaction rate constants for various steps in methane oxidation. The activation energy was both temperature and coverage dependent via the UBI-QEP method. A comprehensive reaction mechanism including methane, CO, formaldehyde and methanol was proposed. The methane dissociative adsorption was separated into four reversible, elementary steps.

NO reduction over platinum had been extensively studied with reducing agents such as H_2 , CO, CH_4 , propane and propene [25,26]; H_2 was the most efficient while CH_4 was the least efficient. When hydrogen was used as the reducing agent, NO was reduced to NH_3 [27,28], N_2 [28], and slight amounts of N_2O [27]. N_2O formation is favored when NO is reduced by CO [27] and NH_3 [29]. The primary role of hydrogen is to keep the catalyst surface clean by react-

ing with surface oxygen [30], exposing more vacant sites for the adsorption of NO. Meanwhile, a mechanism [31] suggested that adsorbed NO dissociated to surface nitrogen $\text{N}(\cdot)$ and surface oxygen $\text{O}(\cdot)$ with the promotion of vacant Pt sites.

In this paper, we describe a microkinetic model for the TWC applied to natural gas engine exhaust. Due to the lack of microkinetic models of methane oxidation over palladium, notably a lack of a comprehensive mechanism including carbon monoxide, methanol, formaldehyde, we chose to build our TWC model on a platinum reaction mechanism. To create our model, published methane oxidation and NO reduction mechanisms on platinum were combined and modified to fit experimental data while maintaining thermodynamic consistency. The resulting mechanism was used to simulate a commercial TWC [9] applied to reducing the emissions from a natural gas engine over a wide range of air to fuel ratios.

2. Mathematical model

The mass balance for the adsorbed species on the solid phase are obtained by assuming competitive adsorption of all species. The adsorption of each species on the catalyst, represented here as a change in species surface coverage (θ_i), at steady state can be calculated as follows:

$$\frac{\partial \theta_i}{\partial t} = 0 \quad (1)$$

$$\frac{\partial \theta_i}{\partial t} = \mathfrak{R}_{\text{adsorption},i} - \mathfrak{R}_{\text{desorption},i} + \sum_j \mathfrak{R}_{\text{reaction},j} \quad (2)$$

The surface coverage of vacant sites is defined as θ_v :

$$\theta_v = 1 - \sum \theta_i \quad (3)$$

The adsorption rate could be calculated as:

$$\mathfrak{R}_{\text{adsorption},i} = \frac{s_i}{\Gamma} \sqrt{\frac{RT}{2\pi M_i}} \left(\frac{T}{T_0}\right)^\beta \exp\left(-\frac{E_{\text{adsorption}}}{RT}\right) C_i \theta_v \quad (4)$$

where s is the sticking coefficient, Γ is the site density of the catalyst, R is the gas constant, T is the absolute temperature, $T_0=300\text{ K}$, β is the temperature component and M is the molecular weight.

The desorption rate is formulated as follows:

$$\mathfrak{R}_{\text{desorption},i} = A_{\text{desorption},i} \left(\frac{T}{T_0}\right)^\beta \exp\left(-\frac{E_{\text{desorption},i}}{RT}\right) \theta_i \quad (5)$$

The Langmuir–Hinshelwood type rate expressions are used to describe reaction rate:

$$\mathfrak{R}_{\text{reaction},j} = A_{\text{reaction},j} \left(\frac{T}{T_0}\right)^\beta \exp\left(-\frac{E_{\text{reaction},j}}{RT}\right) \Pi \theta_i \quad (6)$$

Assuming that flow in the channel can be represented as plug flow, we can write the flowrate for each species as:

$$\frac{dF_i}{dz} = \sum_j \mathfrak{R}_{\text{reaction},j} \Gamma S_m S_{\text{cross}} \quad (7)$$

where: S_m = catalyst surface area, m^2/m^3 , S_{cross} = channel cross section area, m^2 . According to the definition above, at steady state condition, the PFR model equation can be formulated as:

$$\frac{dF_i}{dz} = (\mathfrak{R}_{\text{desorption},i} - \mathfrak{R}_{\text{adsorption},i}) \Gamma S_m S_{\text{cross}} \quad (8)$$

This plug-flow reactor (PFR) model was used to model a single channel in the TWC. The effects of mass transfer limitations in the transport of species to the monolith wall and through the washcoat layer were not considered in our model. To evaluate the validity of

Table 1
Notation.

A	Pre-exponential factor
C	Exhaust gas concentration [mol/m ³]
D _e	Effective diffusivity of gas in the washcoat [m ² /s]
D _f	Molecular diffusivity of the reactant in the fluid phase [m ² /s]
E	Activation energy [kJ/mol]
F	Exhaust flow rate [mol/s]
L	Monolith reactor length [m]
M	Molecular weight [g/mol]
P _t	Transverse Peclet number
R	Gas constant [J/mol/K]
R	Reaction rate [s ⁻¹]
R _{Ω1}	Effective transverse diffusion length for fluid phase [m]
R _{Ω2}	Washcoat thickness [m]
s	Sticking coefficient
S _{ij}	Sensitivity coefficient matrix
S _m	Catalyst surface area [m ² /m ³]
S _{cross}	Channel cross section area [m ²]
t	Time [s]
T	Catalyst temperature [K]
<u>	Average fluid velocity [m/s]
y	Mole fraction
z	Axis coordinate
ε	Porosity
τ	Tortuosity
Γ	Catalyst site density [mol/m ²]
θ	Surface coverage
φ	Thiele modulus
λ	Normalized air to fuel ratio
β	Temperature component
Subscripts	
i	Species
j	Reaction number
v	Vacant sites

Table 2
Exhaust gas mixture composition entering TWC, balanced with N₂.

λ	1.03	1.012	0.992	0.987	0.977	0.953
O ₂ (%)	0.84	0.57	0.41	0.29	0.24	0.29
CO (ppm)	232.39	289.73	858.47	1281.92	2608.51	7960.65
CO ₂ (ppm)	94444	96771	95673	94843	94755	92772
H ₂ (ppm)	77.46	96.58	286.16	427.31	869.5	2653.55
H ₂ O (%)	18.3	17.75	19.13	20.18	19.88	18.66
CH ₄ (ppm)	110.67	171.79	239.89	249.69	300.45	317.01
CH ₂ O (ppm)	9.13	9.62	7.87	6.3	4.55	2.52
NO (ppm)	2817.42	2518.59	2189.19	2068.51	1893.25	1399.16
NH ₃ (ppm)	0.49	0.89	0.59	2.51	4.95	1.87
N ₂ O (ppm)	3.35	2.47	1.84	1.6	1.05	0.29

ignoring external mass transfer, the transverse Peclet number in a single channel was calculated according to [32]:

$$P_t = \frac{R_{\Omega 1}^2 <u>}{LD_f} \quad (9)$$

$R_{\Omega 1}$ is the effective transverse diffusion length for fluid phase and the value is taken as half the width of the monolith channel, $<u>$ is the average fluid velocity, L is the monolith length, D_f is the molecular diffusivity of the reactant in the fluid phase. The diffusivity at 400 °C were calculate from the equation developed by Fuller [33]. The diffusivity of CH₄, CO, CH₂O, NO, NH₃ and N₂O are: 8.771×10^{-5} , 8.135×10^{-5} , 7.183×10^{-5} , 7.578×10^{-5} , 10.937×10^{-5} and 7.623×10^{-5} m²/s, respectively. The corresponding calculated Peclet number are 0.7829, 0.8441, 0.9560, 0.9061, 0.6278 and 0.9008. We note that Joshi et al. argued that external mass transport could be ignored when they studied H₂ oxidation on a Pt/Al₂O₃ monolithic catalyst with a Peclet number close to unity [34]. Since our calculated Peclet number is close to one, we assume that the exhaust concentration profile is uniform in the transverse direction in each channel. The assumption

of no internal mass transport limitations in the washcoat layer was tested by calculating the Thiele modulus φ as defined by [32]:

$$\varphi^2 = \frac{kR_{\Omega 2}^2}{D_e} \quad (10)$$

where k is the reaction rate constant, $R_{\Omega 2} = 25 \mu\text{m}$ (assumed washcoat thickness), and D_e is the effective diffusivity of gas in the washcoat as defined below [35]:

$$D_e = \frac{\epsilon}{\tau} 97a \left(\frac{T}{M_i} \right)^{0.5} \quad (11)$$

where ϵ is the porosity, τ is the tortuosity and a is the pore radius. The values are defined below: $\epsilon = 0.41$, $\tau = 8$, $a = 10^{-8}$ m [35]. In this work, we used the corresponding adsorption step reaction rate constant to calculate the six gas species Thiele moduli in the washcoat and the value are listed below: $\varphi_{\text{CH}_4} = 0.31$, $\varphi_{\text{NO}} = 0.62$, $\varphi_{\text{CO}} = 0.68$, $\varphi_{\text{CH}_2\text{O}} = 0.59$, $\varphi_{\text{NH}_3} = 0.68$, $\varphi_{\text{N}_2\text{O}} = 0.0087$. Because the Thiele moduli are far less than one, internal mass transfer limitation can safely be ignored.

Since experimental data showed that the TWC reactor operated at 400 °C, with only 5–10 °C temperature drop measured along the converter [9], we have assumed isothermal conditions in the TWC was operated at a temperature of 400 °C. Each surface species is expressed in Eq. (2) and each gas species is expressed by Eq. (8). Eq. (2) and are coupled together to form the differential-algebraic equations and solved using Matlab solver ode15s. The definitions of all variables are listed in Table 1.

3. Model validation

Reaction parameters for the equations above were obtained from literature sources. However, since these values were typically derived for a system other than the TWC treating natural-gas engine exhaust, it is necessary to test and modify the model so that it can represent this system. To accomplish this, the model

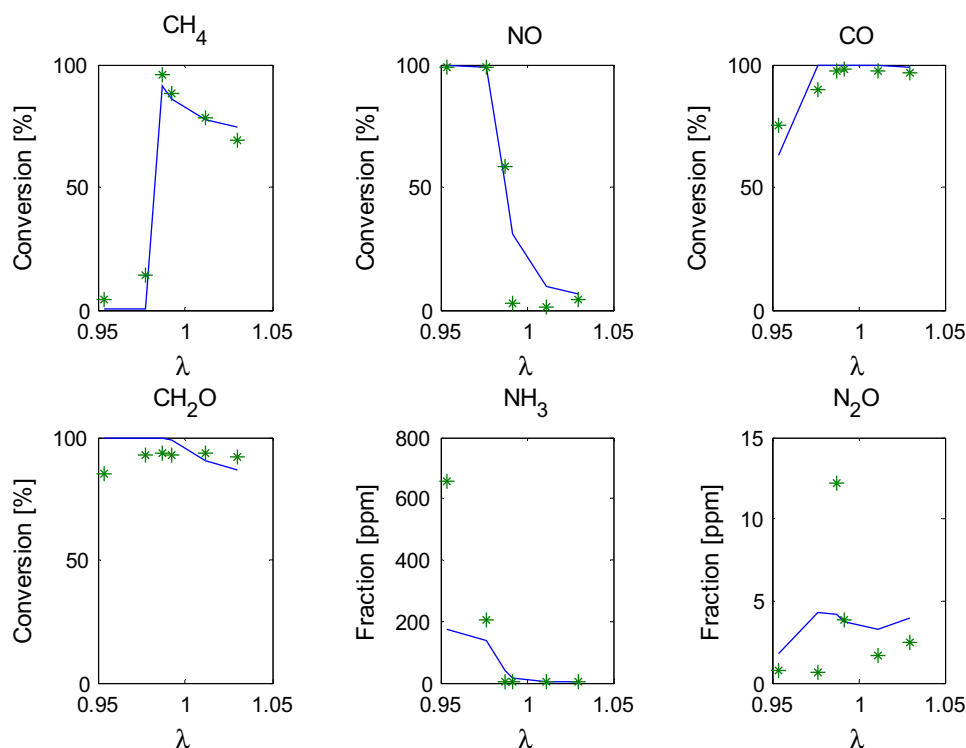


Fig. 1. Simulation of exhaust gas conversion and formation in TWC. Lines are the simulation and symbols are the experimental data.

results were compared to experimental data from Defoort et al. [9]. Their data were obtained by using a commercial TWC consisting of a stainless steel substrate with an alumina (Al_2O_3) and ceria (CeO_2) washcoat with platinum, palladium and rhodium precious metals. The cell density was approximately 75 cells per square centimeter. Four catalyst units were installed, the dimensions of each were $30\text{ cm} \times 40\text{ cm} \times 7.5\text{ cm}$. The nominal temperature was 400°C with a $5\text{--}10^\circ\text{C}$ temperature decrease across the catalyst. This catalyst was placed downstream of a Superior 6G-825 four-stroke natural gas engine with six cylinders with a bore and stroke of 25.4 cm . During steady state test, the engine speed and load were held constant and the air to fuel ratio was varied between 0.953 and 1.03. Exhaust flow rate is about $7.4\text{ m}^3/\text{s}$. Oxygen was measured by a Rosemount five-gas analyzer, other compounds of interest were measured using a Nicolet FTIR. H_2 concentrations are assumed to equal one third of the CO concentration [36,37]. Exhaust gas mixture composition are given in Table 2.

4. Results and discussion

4.1. Surface reaction mechanism

The fundamental requirement for the surface reaction mechanism is that it should include both methane oxidation and NO reduction; however a comprehensive and validated mechanism involved these two chemistries is not available in the literature. In this work, we combined the NO reduction mechanism from different researchers [3,38,39] with a validated methane oxidation model [24]. The surface reaction mechanism for C1 and NO reactions are shown in Table 3 and Table 4 respectively. In our surface mechanism for NO reduction, we considered the following products: NH_3 , N_2 , and N_2O . Defoort et al. showed that NO_2 concentration was zero both pre and post of the TWC [9], so reaction steps involving NO_2 were not considered.

One significant challenge for the model developed in this work was the fact that it is being used to simulate both fuel lean and fuel

rich conditions. At fuel rich conditions, the surface is covered by partial oxidation species, CO and H in particular, while at fuel lean conditions, the surface is covered by oxygen, differences in surface coverages will result in differences in how methane interacts with the catalyst [19]. Meanwhile, Chatterjee et al. modeled the CO, C_3H_6 and NO conversion at fuel rich, near stoichiometric and fuel lean condition and pointed out the C_3H_6 conversion was largely over estimate in the fuel rich condition compared to the experimental data. The deviation was explained by the fact that in the rich condition a wide variety of surface species, such as partial oxidation product of C_3H_6 , resides on catalyst surface, which can reduce the oxygen surface coverage and lead to different reaction pathway [3]. To account for this, the activation energy for methane adsorption was written as a function of CO surface coverage differently in the fuel rich and fuel lean condition. The activation energy was represented by: $1.56 + 0.89 \times \theta_{\text{CO}}$ for fuel lean and $1.56 + 30.31 \times \theta_{\text{CO}}$ for fuel rich (θ_{CO} is the initial surface coverage of carbon monoxide). The higher weight factor indicates that the high CO surface coverage at fuel rich condition increases the dissociative adsorption activation energy and will greatly inhibit the adsorption of methane, which leads to a low conversion of methane at fuel rich conditions. Meanwhile, the methane sticking coefficient was increased from 0.1116 to 0.58, which is close to 0.68 proposed by Aghalayam et al. [40]. Similar parameters tuning procedure had been done by Maestri et al. to increasing the methane sticking coefficient on Rh from 0.229 to 0.572 to better predict experimental results [41].

Model predictions as a function of λ are shown in Fig. 1. These results are compared to experimental data obtained by Defoort et al. [9]. As seen in Fig. 1, the simulation can capture all the important trends except that ammonia is under-estimated at one fuel rich condition ($\lambda = 0.953$); however the NH_3 formation trend is predicted, with little ammonia formation at fuel lean conditions and increased amounts as λ shifts from fuel lean to fuel rich conditions. Methane conversion increases as λ decreases to the stoichiometric point from the lean condition and conversion suddenly decreases to about 10% at fuel rich conditions. The cause of the lower methane

Table 3

Surface reaction mechanism for C1 reactions on platinum [24]. Underlined parameters indicate values that were change in this work from the literature values to improve the model fit to experimental data (six reaction parameters had been changed).

No.	Reaction	s/A (1/s ⁻¹)	β	Ea (kcal/mol)
Adsorption				
1	O ₂ + 2* → 2O*	5.42E-2	0.766	0
2	O* → O ₂	4.91E-2	0.25	0
3	CO* → CO ₂	1E0	0	0
4	CO ₂ + * → CO ₂ *	1.95E-1	0.25	0
5	H ₂ + 2* → 2H*	1.29E-1	0.858	0
6	OH* → OH ₂	9.99E-1	2	0
7	H ₂ O* → H ₂ O	1.08E-1	1.162	0
8	H* → H ₂	3.84E-1	1.832	0
9	COOH* → COOH	6.34E-2	-0.089	0
10	HCOO* + 2* → HCOO**	1.46E-1	0.201	0
11	C* → C	1.64E-2	0.156	0
12	CH* → CH ₄	1.35E-2	0.051	0
13	CH ₂ * → CH ₂	4.5E-2	0.118	0
14	CH ₃ * → CH ₃	1.6E-1	-0.099	0
15	CH ₄ + 2* → CH ₃ * + H*	0.58	0.154	1.56 + w × θ _{CO} ^a
16	CH ₃ OH* → CH ₃ OH	3.34E-1	0.258	0
17	CH ₃ O* → CH ₃ O	1.49E-1	0.054	0
18	CH ₂ O* → CH ₂ O	<u>0.7016</u>	0.098	0
19	CHO* → CHO	1.14E-2	0.096	0
20	CH ₂ OH* → CH ₂ OH	5.26E-2	0.233	0
Reaction				
21	CO ₂ * + * → CO* + O*	4.18E10	0.177	26.3
22	CO* + O* → CO ₂ * + *	2.39E11	-0.177	20.6
23	OH* + * → O* + H*	1.95E12	1.872	27.1
24	O* + H* → OH* + *	6.33E12	0.624	8.8
25	H ₂ O* + * → H* + OH*	9.36E12	-0.118	17.8
26	H* + OH* → H ₂ O* + *	9.99E12	-1.049	13.5
27	H ₂ O* + O* → 2OH*	4.32E10	0.082	8.8
28	2OH* → H ₂ O* + O*	1.7E10	0.325	22.7
29	CO ₂ * + H* → CO* + OH*	8.03E8	-0.531	6.0
30	COOH* + * → CO* + OH*	8.43E8	0.024	5.3
31	CO* + OH* → COOH* + *	1.19E9	-0.024	19.1
32	COOH* + * → CO ₂ * + H*	1.06E11	0.549	1
33	CO ₂ * + H* → COOH* + *	9.45E10	-0.549	2.4
34	CO* + H ₂ O* → COOH* + H*	1.01E11	0.492	23.7
35	COOH* + H* → CO* + H ₂ O*	9.07E10	-0.492	5.6
36	CO ₂ * + OH* → COOH* + O*	5.35E10	0.097	26.6
37	COOH* + O* → CO ₂ * + OH*	1.87E11	-0.097	6.9
38	CO ₂ * + H ₂ O* → COOH* + OH*	8.64E10	-0.031	17.5
39	COOH* + OH* → CO ₂ * + H ₂ O*	1.16E11	0.031	11.9
40	CO* + OH* → CO ₂ * + H*	1.25E9	0.531	18.5
41	CO ₂ * + H* → HCOO**	1.12E11	-0.422	18.5
42	HCOO** → CO ₂ * + H*	8.96E10	0.422	0
43	CO ₂ * + OH* + * → HCOO** + O*	6.17E10	0.236	36.8
44	HCOO** + O* → CO ₂ * + OH* + *	1.62E11	-0.236	0
45	CO ₂ * + H ₂ O* + * → HCOO** + OH*	1.02E11	0.095	25.8
46	HCOO** + OH* → CO ₂ * + H ₂ O* + *	9.78E10	-0.095	3
47	CH ₃ * + H* → CH ₄ + 2*	<u>3.012E11</u>	-0.154	<u>3.86</u>
48	CH ₃ * + * → CH ₂ * + H*	1.11E11	0.419	19.7
49	CH ₂ * + H* → CH ₃ * + *	8.99E10	-0.419	17.3
50	CH ₂ * + * → CH* + H*	5.22E10	0.222	9
51	CH* + H* → CH ₂ * + *	1.92E11	-0.222	35.4
52	CH* + * → C* + H*	9.11E10	0.398	31.3
53	C* + H* → CH* + *	1.1E11	-0.398	13.2
54	CH ₃ * + O* → CH ₂ * + OH*	1.97E11	-0.23	10.8
55	CH ₂ * + OH* → CH ₃ * + O*	5.08E10	0.23	26.6
56	CH* + OH* → CH ₂ * + O*	1.1E11	0.414	44.7
57	CH ₂ * + O* → CH* + OH*	9.1E10	-0.414	0
58	C* + OH* → CH* + O*	6.37E10	0.225	27.7
59	CH* + O* → C* + OH*	1.57E11	-0.225	27.5
60	CH ₂ * + H ₂ O* → CH ₃ * + OH*	8.19E10	0.099	14.1
61	CH ₃ * + OH* → CH ₂ * + H ₂ O*	1.22E11	-0.099	12.3
62	CH* + H ₂ O* → CH ₂ * + OH*	1.81E11	0.269	34
63	CH ₂ * + OH* → CH* + H ₂ O*	5.53E10	-0.269	3.3
64	C* + H ₂ O* → CH* + OH*	1.04E11	0.09	15.6
65	CH* + OH* → C* + H ₂ O*	9.61E10	-0.09	29.3
66	CO* + * → C* + O*	2.85E11	0.468	54.9
67	C* + O* → CO* + *	3.51E10	-0.468	0.3
68	CO* + H* → CH* + O*	3.12E11	0.073	45.8
69	CH* + O* → CO* + H*	3.21E10	-0.073	9.3
70	CO* + H* → C* + OH*	4.97E11	-0.168	40.7
71	C* + OH* → CO* + H*	2.01E10	0.168	4.4
72	2CO* → C* + CO ₂ *	5.94E11	0.393	48.8

Table 3 (Continued)

No.	Reaction	s/A (1/s ⁻¹)	β	Ea (kcal/mol)
73	C* + CO ₂ * → 2CO*	1.68E10	-0.393	0
74	CH ₃ OH* + * → CH ₃ O* + H*	7.82E10	0.102	18.8
75	CH ₃ O* + H* → CH ₃ OH* + *	1.28E11	-0.102	4.3
76	CH ₃ O* + * → CH ₂ O* + H*	1.25E11	0.192	0
77	CH ₂ O* + H* → CH ₃ O* + *	8.03E10	-0.192	14.7
78	CH ₂ O* + * → CHO* + H*	<u>2.85E13</u>	0.27	3.6
79	CHO* + H* → CH ₂ O* + *	<u>5.60E13</u>	-0.27	21
80	CHO* + * → CO* + H*	7.11E10	0.33	0
81	CO* + H* → CHO* + *	1.41E11	-0.33	30.8
82	CH ₃ OH* + * → CH ₂ OH* + H*	8.48E10	0.403	8.7
83	CH ₂ OH* + H* → CH ₃ OH* + *	1.18E11	-0.403	14.6
84	CH ₂ OH* + * → CH ₂ O* + H*	1.14E11	-0.104	7.9
85	CH ₂ O* + H* → CH ₂ OH* + *	8.77E10	0.104	2.2
Desorption				
86	2O* → O ₂ + 2*	8.41E12	-0.796	51–320 _O
87	O* → O + *	1.44E13	-0.25	85–160 _O
88	CO* → CO + *	5.66E15	-0.5	40–230 _{CO}
89	CO ₂ * → CO ₂ + *	3.63E12	-0.25	3.6
90	2H* → H ₂ + 2*	7.95E12	-0.001	19.8–60 _H
91	OH* → OH + *	1.44E14	2	63–330 _O + 25
92	H ₂ O* → H ₂ O + *	2.03E12	1.372	10–2.5 + 250 _{OH}
93	H* → H + *	4.37E13	1.890	62–30 _H
94	COOH* → COOH + *	1.12E13	0.089	55.3
95	HCOO** → HCOO + 2*	4.83E12	-0.201	53.0
96	C* → C + *	4.3E13	-0.156	157.7
97	CH* → CH + *	5.22E13	-0.051	157.1
98	CH ₂ * → CH ₂ + *	1.57E13	-0.118	91.6
99	CH ₃ * → CH ₃ + *	4.42E12	0.099	45.3
100	CH ₃ OH* → CH ₃ OH + *	2.11E12	-0.258	9.5
101	CH ₃ O* → CH ₃ O + *	4.73E12	-0.054	37
102	CH ₂ O* → CH ₂ O + *	<u>6.448E13</u>	-0.098	12
103	CHO* → CHO + *	6.21E13	-0.096	55.5
104	CH ₂ OH* → CH ₂ OH + *	1.35E13	-0.233	50

Table 4

Surface reaction mechanism for NO reactions on platinum proposed in this work. Underlined parameters indicate values that were adjusted to improve the model fit to experimental data.

NO.	Reaction	s/A (1/s ⁻¹)	β	E(kJ/mol)
Adsorption				
105	NO* → NO	0.85 [3]	0	0
106	NH ₃ * → NH ₃	1 [39]	0	0
107	N ₂ O + 2* → NO* + N*	0.01 [38]	0	<u>23</u>
Reaction				
108	NO* + * → N* + O*	<u>9E14</u>	0	107.8 [38]
109	N* + O* → NO* + *	1.005E13[38]	0	168
110	N* + N* → N ₂ + 2*	1.005E13[38]	0	<u>81.9</u>
111	N* + 3H* → NH ₃ *	2.005E16	0	<u>69</u>
112	NH ₃ * + 3* → N* + 3H*	<u>1.005E12</u>	0	<u>110.2</u>
Desorption				
113	NO* → NO + *	<u>1.005E14</u>	0	<u>100</u>
114	NH ₃ * → NH ₃ + *	<u>1.06E16</u>	0	<u>88.4</u>
115	NO* + N* → N ₂ O + 2*	<u>1.005E11</u>	0	<u>75.8</u>

conversion at fuel rich conditions is not due to insufficient oxygen in the exhaust since there is still a large amount of oxygen downstream of the converter. Instead, we propose that the higher surface coverage of CO in fuel rich conditions impacts methane conversion. For this reason, we have modeled the methane dissociative adsorption activation energy differently at fuel rich conditions than fuel lean conditions. This approach acknowledges the literature that shows that the methane interaction mechanism is different at fuel rich conditions due to high CO surface coverage [19]. The NO conversion is low at fuel lean conditions due to excessive oxygen and a limited amount of reducing agents, while as λ decreases, NO conversion gradually increases until the stoichiometric point, at which point there is a step change in NO conversion to 100%. The formaldehyde conversion is consistently high at all conditions while CO conversion decreases to 63.07% at fuel rich condition (λ = 0.953) with the CO mole fraction (7960 ppm) tripling compared to the next

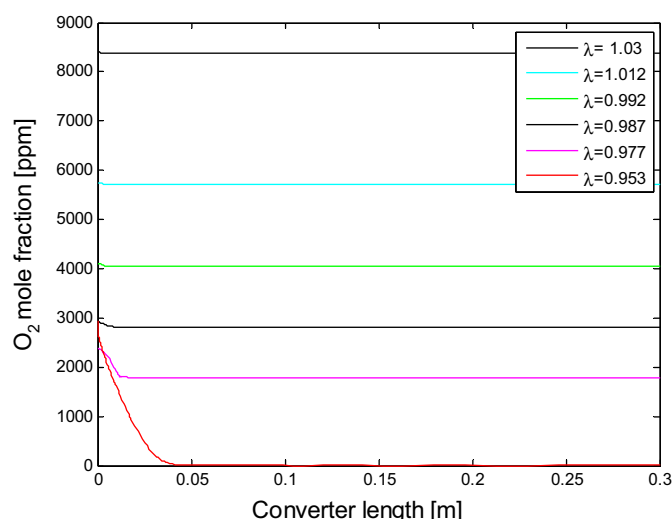


Fig. 2. Oxygen mole fraction in exhaust mixture as a function of converter length at various air to fuel ratio.

data point ($\lambda = 0.977$). N_2O mole fraction did not exhibit a noticeable change after flowing through the converter. The mole fraction is several ppm except one point that is over 10 ppm.

Fig. 2 compares the simulated oxygen concentrations as a function of position in the catalytic converter for different λ 's. This figure shows that when $\lambda = 0.953$, the oxygen concentration gradually decreases and reaches zero at about 0.05 m. It is notable that conversion of oxygen is much higher than that in the experimental data (20.68%). Meanwhile, the corresponding CO conversion is 63.07% which is slightly under predicted. We can make two conclusions based on the simulation results. First, the CO conversion at fuel rich conditions is not as high as that at fuel lean conditions since there is insufficient oxygen for complete oxidation of CO. Second, CO conversion is slightly under predicted because the consumption of oxygen is overestimated. When $\lambda = 0.977$, oxygen concentration decreases initially and then remains at a high concentration through the rest of the converter. The remaining oxygen was sufficient to cause the CO conversion to be higher than that found experimentally.

4.2. Simulated exhaust compositions

Figs. 3 and 4 depict the exhaust composition along the catalyst converter at fuel lean ($\lambda = 1.03$) and fuel rich ($\lambda = 0.977$) compositions, respectively. As seen in these figures, O_2 , CH_4 , CO, CH_2O and NO concentration decrease along the converter, while the CO_2 , NH_3 , N_2O , N_2 concentration increase along the converter. This trend is consistent with experimental observations and represent the general chemistry happening in the catalytic converter. Even though the N_2 concentration is not available in the experimental data, based on the nitrogen mass balance, we can determine that N_2 was produced in the NO reduction process. For both compositions, all reaction chemistry is essentially complete by 0.1 m: only minor changes in gas phase compositions are noted past that point.

4.3. Simulated surface coverages

The calculated surface coverage of all species in both fuel lean ($\lambda = 1.03$) and rich ($\lambda = 0.977$) conditions are shown in **Fig. 5**. OH^* and H_2O^* are the dominant species on the Pt surface for both conditions because the H_2O concentration is about 19% in the exhaust. NO surface coverage exhibits a steeper decrease at the entrance of TWC at the fuel rich condition than that at fuel lean condition indicated that NO^* was converted along the converter which is

consistent with the observation that NO conversion is higher at fuel rich conditions. The N^* surface coverage is higher in the fuel rich condition, which results from higher conversion of NO through decomposition into N^* and O^* . Meanwhile, it can be seen that H^* surface coverage increases as λ shifts from lean to rich. The high N and H surface coverage in the fuel rich condition lead to the higher NH_3 surface coverage at fuel rich condition, and ultimately higher amounts of NH_3 in the exhaust under fuel rich condition. For the fuel rich condition, it can be seen that the coverage of vacant sites initially increases at the entrance of the converter then decreases, while for the fuel lean condition, vacant sites coverage continuously decrease along the converter. The trend for fuel rich conditions can be attributed to the removal of adsorbed CO near entrance of the converter, followed by adsorption of H_2O later in the converter after the major reactions are complete. The vacant sites surface coverage is consistently higher in the fuel rich condition than that in the fuel lean condition. More vacant sites would promote the adsorption of NO, leading to higher NO conversion under fuel rich conditions, but this does not help explain why the experimentally measured methane conversion is low at fuel rich conditions. CO coverage decreases as the reactants progress through the reactor for both conditions, while the initial CO surface coverage at fuel rich condition is much higher than that in the fuel lean condition due to the 10 times higher gas concentration than that in the fuel lean condition. The higher CO surface coverage under fuel rich conditions was taken as the factor that increased the methane dissociative adsorption activation energy to explain the low conversion at fuel rich conditions. High CO surface coverage under fuel rich condition would promote NO^* decomposition by removing O^* .

NO conversion exhibited an opposite trend compared to methane: the NO conversion is relatively high at fuel rich conditions, but it rapidly decreases in the transition from fuel rich to lean conditions, finally reaching a low value (<10%) for $\lambda = 1.03$. Methane, CO and H_2 are all potential reducing agents to convert NO to N_2 and NH_3 . However, R108 ($NO^* + ^* \rightarrow N^* + O^*$) indicated that the adsorbed NO further decomposes to N^* and O^* , and then reducing agents CO^* and H^* can react with the O^* (R22 and R24), leaving vacant sites which also explained why the vacant sites initially increased in the fuel rich conditions.

To investigate NO chemistry, simulations were performed by omitting surface O^* generation from R108 in Eq. (2). These simulations showed that NO conversion and vacant sites surface coverage increased, which indicated that oxygen inhibited the NO reduction by taking the vacant sites for NO adsorption and further decomposition. A similar conclusion was reached by Koop and Deutschmann, who found that CO and C_3H_6 inhibited the oxidation of NO by blocking the adsorption sites for the dissociative adsorption of oxygen [2]. As the NO conversion decreased, NH_3 formation decreased correspondingly, which indicated that NH_3 formed from the precursor NO and this reaction occurred in the TWC, not during fuel combustion in the engine [42].

4.4. Thermodynamic consistency

To check the thermodynamic consistency of the kinetic parameters of the whole mechanism, the reaction enthalpy and entropy of elementary reaction were related to activation energy and pre-exponential factor of a given forward and backward reaction [43]

$$\Delta H_j = E_j^f - E_j^b \quad (12)$$

$$\frac{A_j^f}{A_j^b} = e^{\frac{\Delta S_j}{R}} \quad (13)$$

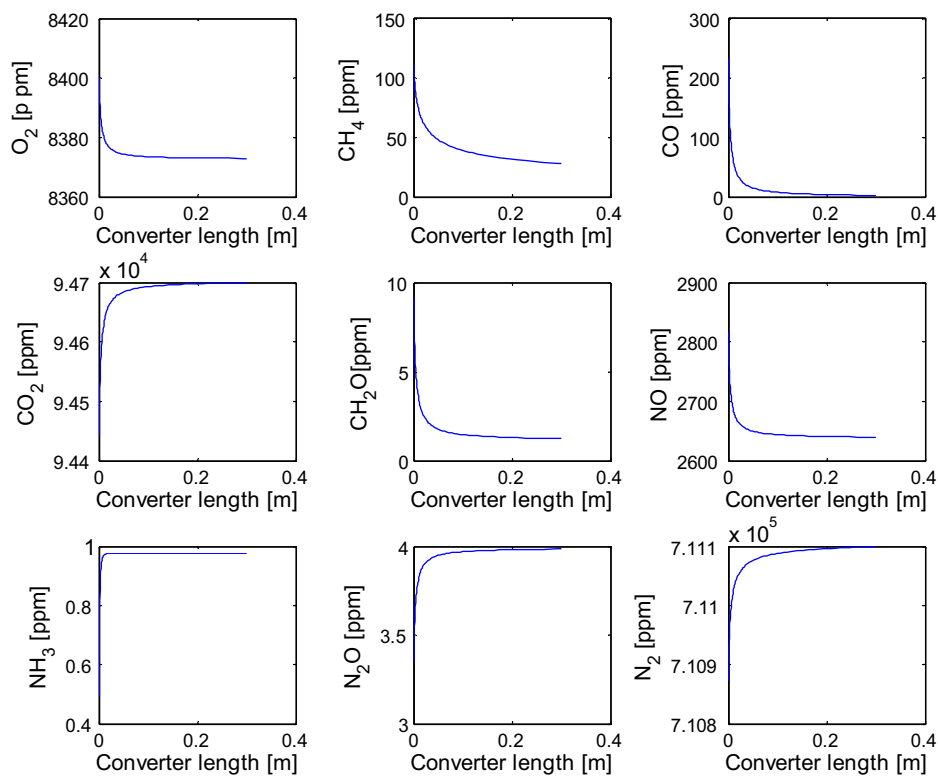


Fig. 3. Exhaust composition as a function of position in the catalytic converter with a fuel lean inlet mixture ($\lambda = 1.03$).

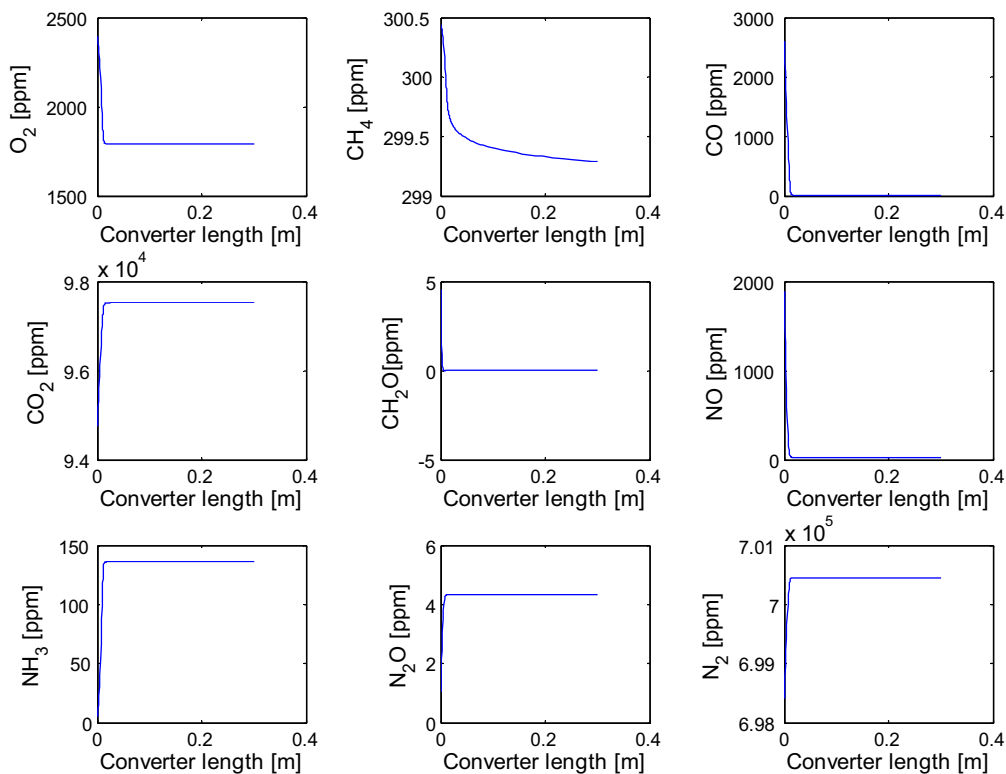


Fig. 4. Exhaust composition as a function of position in the catalytic converter with a fuel rich inlet mixture ($\lambda = 0.977$).

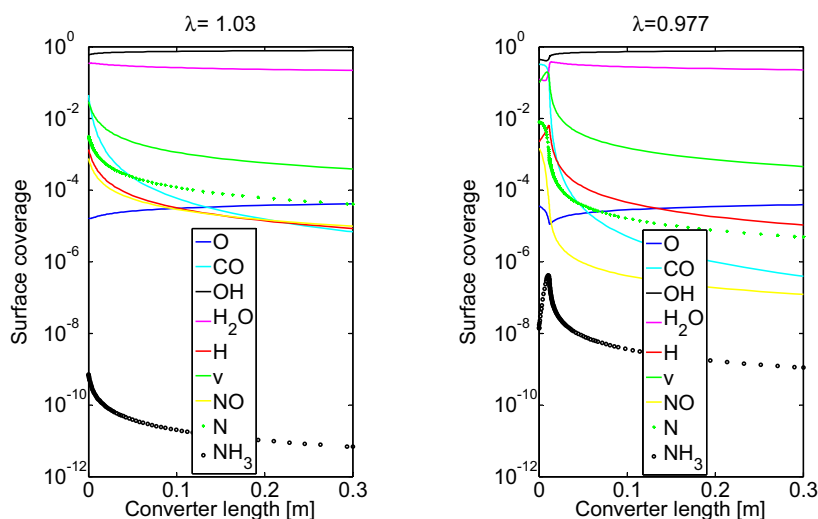


Fig. 5. Simulated surface coverage on catalyst surface as a function of converter length at various air to fuel ratio, v represents the vacant sites. Fuel lean condition (left, $\lambda = 1.03$) and fuel rich condition (right, $\lambda = 0.977$).

For adsorption, sticking coefficients s_i were used. The pre-exponential factor for the adsorption reaction is given as [44]:

$$A_{i,\text{sticking}} = s_i \left(\frac{RT}{2\pi M_i} \right)^{\frac{1}{2}} \quad (14)$$

The original C1 mechanism used to develop our microkinetic model is thermodynamically consistent [24]. In order to simulate TWC performance, the pre-exponential factor of both forward and backward reactions were perturbed by the same order to maintain thermodynamic consistency. For example, the reaction pair consisting of formaldehyde adsorption (R18) and desorption (R102) were changed in Table 3. The methane dissociation adsorption activation energy was reduced from original value 9 kcal/mol to 1.56 kcal/mol, meanwhile the corresponding methane formation reaction R47 ($\text{CH}_3 + \text{H} \rightarrow \text{CH}_4 + \text{H}_2$) activation energy was decreased by the same amount to maintain thermodynamic consistency.

To ensure thermodynamic consistency for the NO reduction portion of our model, we have calculated enthalpy and entropy changes using a thermodynamic database and compare those values to the values obtained from the activation energies and pre-exponentials in the microkinetic model. For example, for the overall reaction $\text{NO} + 2.5\text{H}_2 = \text{NH}_3 + \text{H}_2\text{O}$, enthalpy and entropy changes were calculated from the GRI-Mech thermochemical database, giving values of ΔH of -90.58 kcal/mol and ΔS of -37.25 cal/(mol K) at 300 K. By summing the activation energies and pre-exponentials of the individual surface reaction steps and using Eqs. (10) and (11), values for ΔH and ΔS were found to be -89.13 kcal/mol and -37.23 cal/(mol K), respectively. For the second gas phase reaction $\text{N}_2\text{O} + 0.5\text{O}_2 = 2\text{NO}$, the same calculations was carried out. In the gas phase, ΔH and ΔS are 24.12 kcal/mol and 23.64 cal/(mol K), respectively; based on the model, they are 24.12 kcal/mol and 22.79 cal/(mol K). Thus, we proposed a thermodynamically consistent surface reaction for the natural gas engine exhaust in TWC.

4.5. Sensitivity analysis

Since the reaction mechanism is large, it is difficult to identify the important reaction steps influencing a response without a systematical method [45]. In this work, we examine sensitivity coefficients when determining the important reactions. The pre-exponential factor (A) was chosen as the parameter and the exit

emission mole fraction (y) as the response. The sensitivity coefficient is defined as:

$$S_{i,j} = \frac{\partial (\ln y_i)}{\partial (\ln A_j)} = \frac{\ln y_i^0 - \ln y_i}{\ln A_j^0 - \ln A_j} \quad (15)$$

Here, A_j^0 and A_j denote the initial pre-exponential factor and perturbed pre-exponential factor, respectively. The pre-exponential factor of each elementary reaction was perturbed by a same factor. y_i^0 and y_i are the species mole fraction using A_j^0 and A_j , respectively. In this calculation, exit exhaust mole fraction was chosen as the response for sensitivity coefficient calculations [46].

Fig. 6 shows the reactions that are important to the six key exhaust species. The sensitivity analysis was performed for each exhaust by decreasing the pre-exponential factor of each elementary reaction by a factor of 1.2. The sensitivity coefficient are further normalized to the largest absolute value in each data set (NSC), so the maximum NSC value in each set is 1.0. With a threshold value of 0.16 for the absolute value, as shown in the figure, methane, NO and CO are all most sensitive to the adsorption steps (R15, R105 and R3, respectively). Aghalayam et al. modelled the methane oxidation on platinum and sensitivity analysis also showed that methane conversion is most sensitive to the methane dissociative adsorption step [40]. These species are converted in the TWC, so it makes sense that their adsorption plays the biggest role in their chemistry. However, Figure 6 also shows how these three species are impacted by reaction steps involving each other. For example, reaction steps R105 ($\text{NO} + * \rightarrow \text{NO}^*$), R113 ($\text{NO}^* \rightarrow \text{NO} + *$) and R108 ($\text{NO}^* + * \rightarrow \text{N}^* + \text{O}^*$) have noticeable NSC values for methane, NO, and CO. These three steps are for NO adsorption, NO desorption, and decomposition to N^* and O^* , clearly indicating how NO can occupy surface sites that can otherwise be used for methane and CO conversion. In a similar way, CO adsorption has a large impact on methane conversion. Finally, oxygen adsorption (R1) had a noticeable negative impact on NO conversion since the sign is opposite to the NO adsorption (R105). This can be explained by considering that oxygen inhibits NO^* decomposition (R108) on the surface. Formaldehyde conversion is primarily sensitive to the formaldehyde adsorption step R18 ($\text{CH}_2\text{O} + * \rightarrow \text{CH}_2\text{O}^*$), the formaldehyde desorption step R102 ($\text{CH}_2\text{O}^* \rightarrow \text{CH}_2\text{O} + *$) and surface reaction R78 ($\text{CH}_2\text{O}^* + * \rightarrow \text{CHO}^* + \text{H}^*$); however, it has some dependence on NO chemistry due to competitive adsorption. The ammonia and N_2O are most sensitivity to reactions that related to the formation of these two species since both NH_3 and N_2O

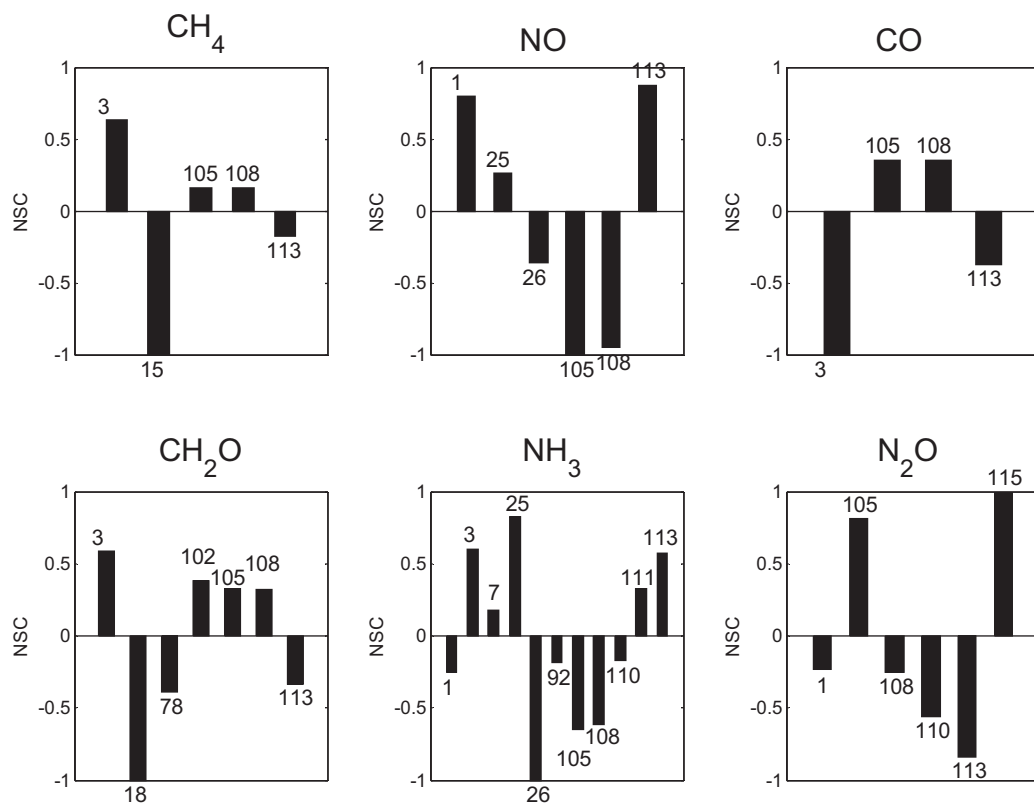


Fig. 6. Sensitivity analysis of CH_4 , NO, CO, CH_2O , NH_3 and N_2O mole fraction with respect to pre-exponential factors at reaction conditions, $\lambda = 1.03$. The numbers are referring to the reactions listed Tables 3 and 4.

are produced within the TWC. R25 ($\text{H}_2\text{O} + \cdot \rightarrow \text{H} + \text{OH} \cdot$) and R26 ($\text{H} + \text{OH} \cdot \rightarrow \text{H}_2\text{O} + \cdot$) both had a noticeable impact on the NH_3 , which indicates that ammonia formation competes with other reactions involving $\text{H} \cdot$. Surface reactions R105 ($\text{NO} + \cdot \rightarrow \text{NO} \cdot$), R108 ($\text{NO} \cdot + \cdot \rightarrow \text{N} \cdot + \text{O} \cdot$) and R113 ($\text{NO} \cdot \rightarrow \text{NO} + \cdot$), which are all related to the NO surface concentration, are shown in the ammonia and N_2O sensitivity analysis, since NO is the nitrogen source for their formation. R111 ($\text{N} \cdot + 3\text{H} \cdot \rightarrow \text{NH}_3 \cdot$) is the surface reaction that leads to ammonia formation on the surface.

The sensitivity analysis provides information not only on which reactions are important, but also suggest which reactions should be modified to better capture the experimental results. The reaction parameters reported in Tables 2 and 3 were found using sensitivity analysis to decide which reaction parameters should be modified.

5. Conclusion

A detailed and thermodynamically consistent surface reaction mechanism capable of modelling all the key reactions in the TWC applied to treat exhaust from a natural-gas engine was developed by selecting the elementary-step reactions from the literature. By adjusting six of the 104 reaction steps in C1 mechanism and proposing a NO reduction mechanism, the model was able to predict the major trends in CH_4 , NO, and CO conversion and NH_3 and N_2O production over a wide range of fuel to air ratios. A comprehensive reaction mechanism and sensitivity analysis to determine the important reaction steps are essential for the modeling process and predicting the experiment results. With a fuel rich feed ($\lambda = 0.953$), CO conversion is a little underpredicted due to the high conversion of O_2 which leads to insufficient oxygen for further CO oxidation. Conversion of NO is high at fuel rich conditions because reducing agents such as CO and H_2 can remove the $\text{O} \cdot$ and promote the decomposition of $\text{NO} \cdot$ into $\text{N} \cdot$ and $\text{O} \cdot$, which accelerates the con-

version of NO. In fuel lean conditions, CO was almost completely converted, and excessive oxygen further decreased the surface CO concentration. Because of this, dissociative adsorption of methane is less inhibited by the surface CO. NO conversion is low at fuel lean conditions because NO decomposition on the surface was inhibited by the high concentration of oxygen and also by less reducing agent to remove $\text{O} \cdot$. A small variation of the air-fuel ratio had a great impact on the simulated converter performance, showing the importance of maintaining the air to fuel ratio in a narrow stoichiometric window to obtain a high emission removal efficiency. Sensitivity analysis indicated that adsorption steps have the largest impact on removing methane, NO, CO and formaldehyde. Ammonia and N_2O , which are produced in the TWC, are sensitive to the reactions that relate to their formation, such as R25, R26, R108 and R111 for NH_3 and R1, R108 and R115 for N_2O . In addition, the R105 and R108 have large NSC value means that NO adsorption and decomposition steps affect production/conversion of all six important species.

Acknowledgements

This work has been supported by Pipeline Research Council International, Inc. through grant# PR-266-14200. The assistance of Dr. Daniel Olsen is gratefully acknowledged for sharing his experimental data and for helpful discussions. We would also like to thank SoCal Gas for providing support and guidance.

References

- [1] G.C. Koltsakis, A.M. Stamatelos, *Prog. Energy Combust. Sci.* 23 (1997) 1–39.
- [2] J. Koop, O. Deutschmann, *Appl. Catal. B* 91 (2009) 47–58.
- [3] D. Chatterjee, O. Deutschmann, J. Warnatz, *Faraday Discuss.* 119 (2002) 371–384.

- [4] ExxonMobile, <http://corporate.exxonmobil.com/en/energy/energy-outlook> (2015).
- [5] M. Shelef, R.W. McCabe, *Catal. Today* 62 (2000) 35–50.
- [6] A. Trovarelli, *Catal. Rev.* 38 (1996) 439–520.
- [7] P. Kumar, I. Makki, J. Kerns, K. Grigoriadis, M. Francheck, V. Balakotaiah, *Chem. Eng. Sci.* 73 (2012) 373–387.
- [8] G.C. Koltsakis, A.M. Stamatelos, *Chem. Eng. Sci.* 54 (1999) 4567–4578.
- [9] M. Defoort, D. Olsen, B. Willson, *Int. J. Eng. Res.* 5 (2004) 115–122.
- [10] R. Burch, D. Crittle, M. Hayes, *Catal. Today* 47 (1999) 229–234.
- [11] P. G  lin, M. Primet, *Appl. Catal. B* 39 (2002) 1–37.
- [12] G. Groppi, C. Cristiani, L. Lietti, P. Forzatti, *Stud. Surf. Sci. Catal.* 130 (2000) 3801–3806.
- [13] J.B. Miller, M. Malatpure, *Appl. Catal. A* 495 (2015) 54–62.
- [14] A. Trinchero, A. Hellman, H. Gr  nbeck, *Surf. Sci.* 616 (2013) 206–213.
- [15] M.M. Souza, M. Schmal, *Appl. Catal. A* 281 (2005) 19–24.
- [16] P. Tornia  inen, X. Chu, L. Schmidt, *J. Catal.* 146 (1994) 1–10.
- [17] I. Wierzb  , A. Depiak, *Int. J. Hydrog. Energy* 29 (2004) 1303–1307.
- [18] R. Burch, P. Loader, *Appl. Catal. B* 5 (1994) 149–164.
- [19] M. Lyubovsky, L.L. Smith, M. Castaldi, H. Karim, B. Nentwick, S. Etemad, R. LaPierre, W.C. Pfefferle, *Catal. Today* 83 (2003) 71–84.
- [20] O. Buyevskaya, D. Wolf, M. Baerns, *Catal. Lett.* 29 (1994) 249–260.
- [21] D. Hickman, L.D. Schmidt, *AIChE J.* 39 (1993) 1164–1177.
- [22] O. Deutschmann, R. Schwiedemoch, L.I. Maier, D. Chatterjee, *Stud. Surf. Sci. Catal.* 136 (2001) 251–258.
- [23] R. Schwiedernoch, S. Tischer, C. Correa, O. Deutschmann, *Chem. Eng. Sci.* 58 (2003) 633–642.
- [24] A. Mhadeshwar, D. Vlachos, *Ind. Eng. Chem. Res.* 46 (2007) 5310–5324.
- [25] R. Burch, P. Millington, *Catal. Today* 26 (1995) 185–206.
- [26] S. Poulston, R.R. Rajaram, *Catal. Today* 81 (2003) 603–610.
- [27] H. Abdulhamid, E. Fridell, M. Skoglundh, *Appl. Catal. B* 62 (2006) 319–328.
- [28] I. Nova, L. Lietti, L. Castoldi, E. Tronconi, P. Forzatti, *J. Catal.* 239 (2006) 244–254.
- [29] I. Nova, L. Lietti, P. Forzatti, *Catal. Today* 136 (2008) 128–135.
- [30] T. Szailer, J.H. Kwak, D.H. Kim, J.C. Hanson, C.H. Peden, J. Szanyi, *J. Catal.* 239 (2006) 51–64.
- [31] R. Burch, J. Breen, F. Meunier, *Appl. Catal. B* 39 (2002) 283–303.
- [32] S.Y. Joshi, M.P. Harold, V. Balakotaiah, *Chem. Eng. Sci.* 65 (2010) 1729–1747.
- [33] E.N. Fuller, P.D. Schettler, J.C. Giddings, *Ind. Eng. Chem.* 58 (1966) 18–27.
- [34] S.Y. Joshi, Y. Ren, M.P. Harold, V. Balakotaiah, *Appl. Catal. B* 102 (2011) 484–495.
- [35] L. Mukadi, R. Hayes, *Comput. Chem. Eng.* 26 (2002) 439–455.
- [36] M.A. Toema, *Physics-Based Characterization of Lambda Sensor Output to Control Emissions from Natural Gas Fueled Engines*. PhD diss., Kansas State University, 2010.
- [37] H. Yao, Y.Y. Yao, *J. Catal.* 86 (1984) 254–265.
- [38] J. Xu, R. Clayton, V. Balakotaiah, M.P. Harold, *Appl. Catal. B* 77 (2008) 395–408.
- [39] J. Vajo, W. Tsai, W. Weinberg, *J. Phys. Chem.* 89 (1985) 3243–3251.
- [40] P. Aghalayam, Y.K. Park, N. Fernandes, V. Papavassiliou, A. Mhadeshwar, D.G. Vlachos, *J. Catal.* 213 (2003) 23–38.
- [41] M. Maestri, D.G. Vlachos, A. Beretta, G. Groppi, E. Tronconi, *AIChE J.* 55 (2009) 993–1008.
- [42] N.V. Heeb, A. Forss, S. Br  hlmann, R. L  scher, C.J. Saxer, P. Hug, *Atmos. Environ.* 40 (2006) 5986–5997.
- [43] A.B. Mhadeshwar, H. Wang, D.G. Vlachos, *J. Phys. Chem. B* 107 (2003) 12721–12733.
- [44] M. Saliccioli, M. Stamatakis, S. Caratzoulas, D.G. Vlachos, *Chem. Eng. Sci.* 66 (2011) 4319–4355.
- [45] P. Gokulakrishnan, P. McLellan, A. Lawrence, E. Grandmaison, *Chem. Eng. Sci.* 60 (2005) 3683–3692.
- [46] S. Vajda, P. Valko, T. Turanyi, *Int. J. Chem. Kinet.* 17 (1985) 55–81.